



**HAL**  
open science

# Multiscale physical-chemical analysis of the impact of fracture networks on weathering: Application to Nickel redistribution in the formation of Ni-laterite ores, New Caledonia

Sylvain Favier, Yoram Teitler, Fabrice Golfier, Michel Cathelineau

► **To cite this version:**

Sylvain Favier, Yoram Teitler, Fabrice Golfier, Michel Cathelineau. Multiscale physical-chemical analysis of the impact of fracture networks on weathering: Application to Nickel redistribution in the formation of Ni-laterite ores, New Caledonia. *Ore Geology Reviews*, 2022, 147, pp.104971. 10.1016/j.oregeorev.2022.104971 . hal-03844085

**HAL Id: hal-03844085**

**<https://hal.univ-lorraine.fr/hal-03844085>**

Submitted on 8 Nov 2022

**HAL** is a multi-disciplinary open access archive for the deposit and dissemination of scientific research documents, whether they are published or not. The documents may come from teaching and research institutions in France or abroad, or from public or private research centers.

L'archive ouverte pluridisciplinaire **HAL**, est destinée au dépôt et à la diffusion de documents scientifiques de niveau recherche, publiés ou non, émanant des établissements d'enseignement et de recherche français ou étrangers, des laboratoires publics ou privés.



Distributed under a Creative Commons Attribution - NonCommercial - NoDerivatives 4.0 International License

1 **Multiscale physical-chemical analysis of the impact of fracture**  
2 **networks on weathering: Application to Nickel redistribution in the**  
3 **formation of Ni-laterite ores, New Caledonia**

4

5 **Sylvain Favier<sup>a</sup>, Yoram Teitler<sup>a</sup>, Fabrice Golfier<sup>a</sup>, Michel Cathelineau<sup>a</sup>**

6 <sup>a</sup>Université de Lorraine, CNRS, GeoRessources, 54000 Nancy, France

7 Sylvain Favier (corresponding author)

8 [sylvain.favier@univ-lorraine.fr](mailto:sylvain.favier@univ-lorraine.fr)

9 Yoram Teitler

10 [yoram.teitler@univ-lorraine.fr](mailto:yoram.teitler@univ-lorraine.fr)

11 Fabrice Golfier

12 [fabrice.golfier@univ-lorraine.fr](mailto:fabrice.golfier@univ-lorraine.fr)

13 Michel Cathelineau

14 [michel.cathelineau@univ-lorraine.fr](mailto:michel.cathelineau@univ-lorraine.fr)

## 15 Abstract

16 Supergene processes related to downward water migration and dissolution of primary minerals in the  
17 New Caledonian peridotites result in Ni enrichment at the bottom of the lateritic profile near bedrock.  
18 However, the combined effects of relief, lateral fluid flow, and complex inherited discontinuity  
19 networks filled by serpentine generate a more complex Ni distribution than a simple flat horizon. In  
20 surficial environments, fluid flow and mass transfer are not limited to the vertical scale; they can also  
21 be related to lateral fluid circulation and local drainage along damage zones in the vicinity of faults. In  
22 this study, we present new structural, petrophysical and geochemical data for core samples to shed  
23 light on the impact of a fracture network on the alteration and progression of the Ni-enrichment front  
24 during weathering. The analysis of element redistribution by XRF mapping coupled with fracture  
25 extraction from computed tomography (CT) establishes that the serpentine fracture network  
26 comprises sets of sub-orthogonal fractures whose orientations are potentially determined by pre-  
27 existing magmatic foliation. The progression of the olivine dissolution front leads to the redistribution  
28 and concentration of Ni into the serpentine fracture network as secondary Mg-Ni talc-like phases. The  
29 increase in porosity from <1% in the bedrock to >10% in the saprock is mainly driven by the formation  
30 of nanopores. Nanoporosity may control the development of the weathering front and the  
31 redistribution of Ni by small-scale diffusion. Structural and geochemical characteristics identified at  
32 the sample scale are analogous to those observed on the larger scale of the outcrop and deposit. Scale  
33 invariance in the structural organization and geochemical evolution indicates the potential upscaling  
34 of the processes involved in the redistribution of Ni.

35

## 36 Keywords

37 Fractures, Multiscale, Weathering, Nickel

## 38 I. Introduction

39 Ni-laterite deposits in New Caledonia represent 7 % of the global mine production in 2021 (USGS,  
40 2022). Laterite is a surficial formation developed after the deep weathering of rocks under a hot, wet  
41 tropical climate. The rainwater leaches most of the soluble elements, which leads to the residual  
42 concentration of more insoluble elements such as Al, Fe or Ni (Best, 2015). In the New Caledonian  
43 mining district, laterites originated from the weathering of ultramafic rocks consisting of relics of the  
44 obducted Peridotite Nappe during the Eocene (Chevillotte, 2005; Gautier et al., 2016; Sevin et al., 2014;  
45 Trescases, 1975). The downward migration of meteoric waters leached most elements from the  
46 peridotites (Mg, Ni, Si) except iron. Waters are saturated at depth with respect to newly-formed Si-  
47 Mg-Ni minerals in the saprolite (Butt and Cluzel, 2013; Freyssinet et al., 2005; Golightly, 2010; Haldar,  
48 2017). During this process, Ni is trapped in Fe-(oxy)-hydroxides in the oxide zone and phyllosilicates in  
49 the saprolite ore (Dublet et al., 2012; Fritsch et al., 2016; Santoro et al., 2022; Villanova-de-Benavent  
50 et al., 2014). Ni is redistributed towards the bottom of the laterite profile during laterite formation due  
51 to the goethite dissolution-recrystallisation process, so-called the goethite ageing (Dublet et al., 2015).  
52 The tectonic uplift enhanced the downward redistribution process from the oxide zone toward the  
53 saprolite ore. Indeed, rejuvenating the topography and lowering the water tables maintained the  
54 drainage conditions required to redistribute elements and differentiate the laterite profile (Maurizot  
55 et al., 2020). Therefore, the competition between tectonic uplift and weathering rate controls the  
56 dominant ore type in Ni lateritic deposits. Oxide ore formation is favored in poorly uplifted areas  
57 dominated by weathering, whereas saprolite ore formation occurs in more uplifted areas (Butt and  
58 Cluzel, 2013; Maurizot et al., 2020). However, a pure “*per descensum*” model fails to fully explain the  
59 Ni heterogeneities observed in the saprolite (Quesnel et al., 2017), where several fissure infillings with  
60 distinct habitus and mineral-chemistry are found (Cathelineau et al., 2016, 2017). The Ni concentration  
61 in the saprolite ore is generally around 2 wt% and locally up to 5 wt.% (Butt and Cluzel, 2013; Tauler et  
62 al., 2017). It results from the contribution of several Mg-Ni phyllosilicates (predominantly talc-like)  
63 forming the so-called “garnierite ore”, whose Ni contents vary from a few % up to 30 wt.% Ni

64 (Cathelineau et al., 2017). This complexity results from a multiphase redistribution model based on the  
65 pre-concentration of Ni in fractures. The garnierite ore is subsequently affected by the downward  
66 migration of a dissolution front guided by fracture networks at the outcrop scale (Cathelineau et al.,  
67 2017). Fu et al. (2018) suggested that the origin of the “garnierite ore” is closely linked to the  
68 preferential flow regime in conduits and is often associated with dissolution pipes. Iseppi et al. (2018)  
69 pointed out the structural control at the deposit- to massif- scale on the Ni remobilization. Inherited  
70 fractures control erosion at a massif scale and act as drains and permeability walls due to the  
71 impermeable serpentine coating at the deposit scale. Myagkiy et al. (2019) highlighted the effect of  
72 topographic slope and occurrence of fractures on Ni redistribution through the 2D modelling of  
73 reactive transport.

74 More generally, whatever the lithology, fractures may be organized as networks following fractal  
75 organization, meaning that fracture networks show the same spatial distribution at different scales  
76 (Basirat et al., 2019; Roy et al., 2007). Consequently, the structural organization observed at outcrop  
77 and larger scales should also be found at a smaller scale. In New Caledonia, fracture networks play an  
78 essential role in the Ni redistribution at the saprolitic level at the outcrop scale. There, the potential  
79 fractal organization of the fracture network would imply that Ni redistribution processes may present  
80 similarities at different scales. Furthermore, scaling laws have been widely applied to describe fracture  
81 network statistical properties at different scales (Afshari Moein et al., 2019; Bonnet et al., 2001; Bour,  
82 2002; Masihi and King, 2008). The impact of scaling laws on fluid flow or seismic hazard has been widely  
83 explored (Allègre et al., 1982; de Dreuzy et al., 2012; Hatton et al., 1993), but the applicability to ore  
84 deposits formation remains to be addressed. The upscaling of Ni mineralization processes from the  
85 core to the field scale would be of prime interest for mine exploration. Although structural data are  
86 generally available at the regional and deposit scale (Jeanpert et al., 2019; Quesnel et al., 2017),  
87 microstructural, petrophysical or geochemical characterization at the sample scale is often lacking.

88 This paper investigates the impact of fracture networks at the sample scale on Ni redistribution when  
89 parent rocks are affected by the progression of the silicate dissolution front. Representative core

90 samples of the dissolution front were collected from the Cagou pit (Koniambo Massif). Structural,  
91 petrophysical and geochemical features identified at the sample scale are compared to those  
92 documented at the scale of outcrops and mine workings, allowing discussion on the potential upscaling  
93 of the genetic processes for a correct understanding of the factors controlling the ore geometry.

94

## 95 Geological settings

96 The “Grande Terre” island of the New Caledonian archipelago, located in SW Pacific (Figure 1.a),  
97 consists of ca. 30% of ultramafic rocks, which are relics of the obducted Peridotite Nappe on the  
98 continental Norfolk Ridge during the Eocene period (Cluzel et al. 2001). The Peridotite Nappe is  
99 nowadays observed in the “Massif du Sud” and in klippe mainly along the West Coast, including the  
100 Koniambo Massif. Main fracture directions in the ultramafic rocks strike N130°-N150°, parallel to the  
101 main elongation direction of the island, which is commonly thought to be the obduction azimuth.  
102 However, several other sets of fractures striking N0°, N45°, and N90° at the island scale are related to  
103 later deformation stages, including the Miocene extensional tectonics (Lagabrielle et al., 2005).

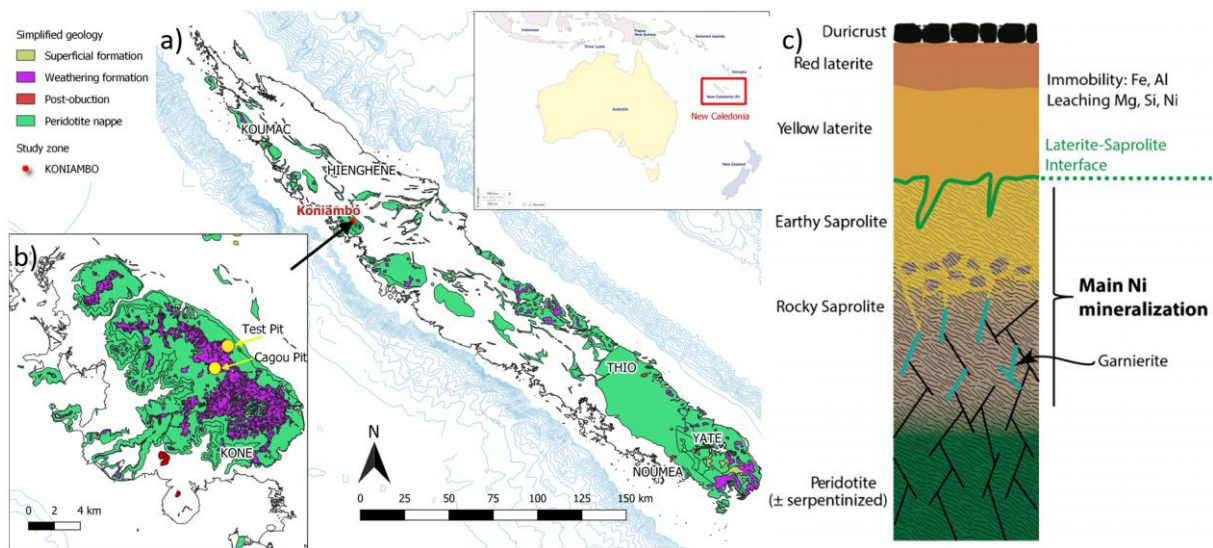
104 After the obduction (late Oligocene), the peridotite is affected by deep weathering in a hot and humid  
105 climate, ending with a thick lateritic profile (Sevin et al., 2012). In the laterite profile, several domains  
106 can be outlined, which from base to top are (i) a saprolite horizon resulting from the progressive  
107 dissolution of the variably serpentinized peridotite bedrock mainly consisting of silicates (olivine),  
108 allowing the precipitation of phyllosilicates and goethite (detailed explanation of the chemical  
109 reactions are given in Butt and Cluzel (2013) and Myagkiy et al. (2017)), and of (ii) an oxide ore which  
110 is the final weathering stage, resulting from the dissolution and leaching of all minerals apart from  
111 immobile goethite (Figure 1.c).

112 The Koniambo Massif (Figure 1.b) is defined by a highly marked relief and poly-directional fracture  
113 network mainly oriented WNW-ESE, NS, NW-SE and NE-SW (Jeanpert et al., 2019; Quesnel et al., 2016).

114 The regolith observed in the massif consists of hectometer-sized patches of laterite profiles of varying

115 thicknesses ranging from a few meters to > 60m (Quesnel et al., 2017). Ni-rich saprolites are mainly  
 116 located on slopes where the oxide ore cover is thin or absent. In contrast, Ni-poor saprolites tend to  
 117 be situated in topographic highs under thick oxide ore cover (Quesnel et al., 2017). The Cagou open  
 118 pit, previously called Pit 207 in previous related studies describing the rock mineralogy (Cathelineau et  
 119 al., 2017, 2016; Muñoz et al., 2019), presents locally preserved oxide ore cover ranging from a few  
 120 meters to 20 m in thickness, and an intense fracture network in the rocky saprolite - bedrock contact  
 121 zone (Quesnel et al., 2016).

122



123

124 *Figure 1 – a) Geological map of New Caledonia. b) Geological setting of Koniambo Massif. c) Typical peridotite-derived*

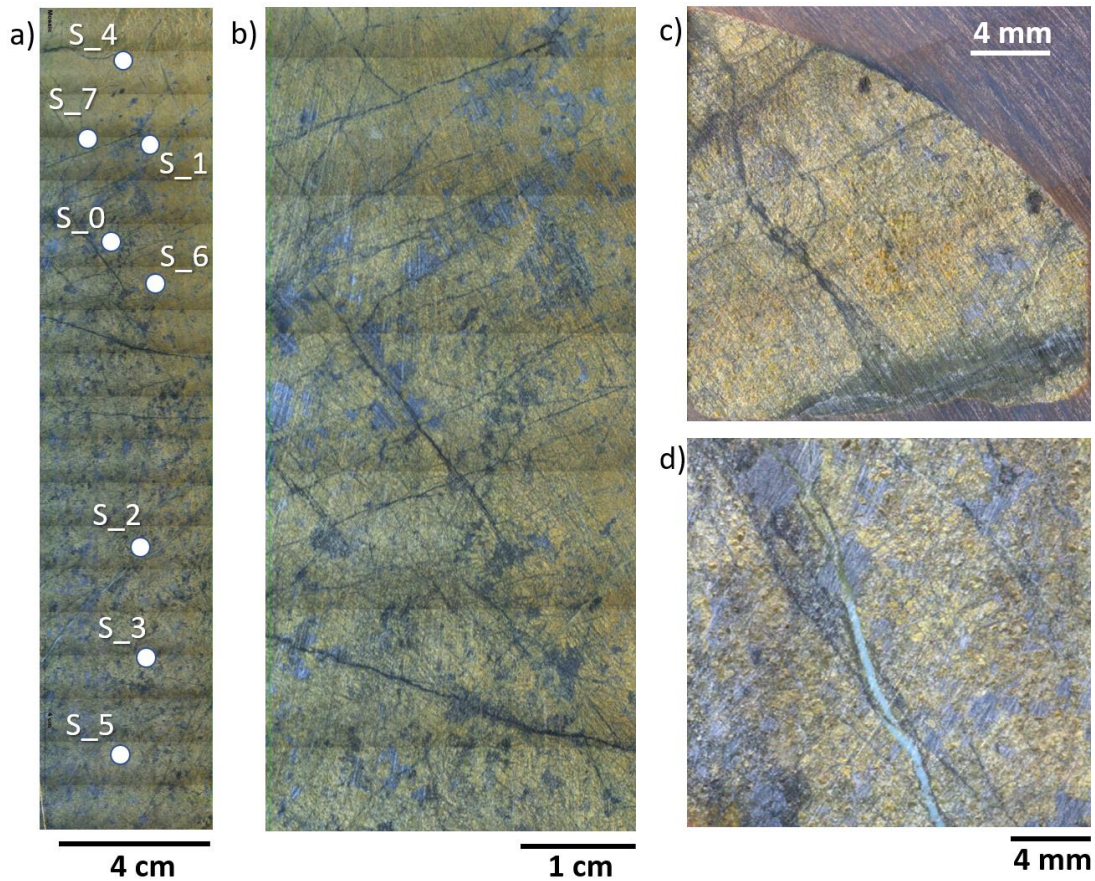
125

*lateritic profile (Quesnel et al. (2017))*

## 126 II. Materials and Methods

127

128 To study the impact of fractures on the weathering front progress at different scales, structural,  
129 petrophysical and geochemical data were collected on a 30 cm-long core sample (Figure 2.a). The 30  
130 cm-long core sample was collected at a depth between 6 m and 6.3 m of a vertical 41 m deep drill hole  
131 in the Cagou Pit (latitude: 20°58'25.163" S, longitude: 164°47'29.683" E, altitude: 755m) (Figure 1.b).  
132 The core sample shows a visible fracture network and an increase in weathering intensity, from the  
133 fresh peridotite at the bottom to the altered peridotite at the top, with a typical brownish colouring  
134 due to goethite. A 32 mm x 73 mm focus on the upper part of the core sample (named S\_0) was used  
135 to describe the analyzed processes at the cm-scale. Various 20 mm x20 mm subsamples from the core,  
136 respectively called S\_1 to S\_7 (Figure 2.a), were also studied to provide data at the mm scale. Since the  
137 drill core is not oriented, all measured orientations are not in situ but relative ones. Yet, the subsamples  
138 are still oriented consistently with the core sample.



139

140 *Figure 2 - Samples used for the study. a) Core sample and the localization of the different subsamples. b) Sample S\_0. c)*

141

*Sample S\_1. d) Sample S\_2.*

## 142 II.1. Structural data acquisition

143 Fractures features and beddings extraction.

144 Structural analysis was based on 3D computed tomography (CT) imaging of the core sample and the

145 sub-sample S\_2 using the Nanotom Phoenix X-ray tomograph (GE) of GeoRessources laboratory. This

146 non-destructive technique provides 3D visualizations of the internal structure of the samples based on

147 the differential absorption of X-rays of the microfracture infillings. CT-scans revealed the structure

148 density linked to differential absorption and were then compared to backscattered-electron (BSE)

149 images obtained on S\_2.

150 The CT scans were treated as image stack to extract fracture geometry using the FIJI software

151 (Schindelin et al., 2012). One of the analytical challenges was the low-density contrast between

152 fractures and the matrix in some areas. Indeed, the mineralogical phases in fractures and matrix mainly

153 consist of light elements such as Si and Mg, with a minor Ni amount in fractures. Depending on the  
154 degree of mineral filling, the fractures appeared slightly darker than the matrix for poorly filled  
155 fractures or slightly brighter for mineralized fractures. The challenge was thus to find a method able to  
156 extract both poorly filled fractures and mineralized fractures from the matrix. Furthermore, the density  
157 of the matrix also changes as a function of the weathering degree, making the extraction of the fracture  
158 network even more challenging and hence the segmentation more complex. The point cloud of the  
159 stack was then extracted and imported into CloudCompare software (GPL software, 2021) to extract  
160 the fracture sets based on their dip/direction value. Finally, planes were adjusted from points using  
161 the Ransac Shape Detection Plugin (Schnabel et al., 2007) and exported to analyze their spatial and  
162 orientation distribution.

163 The orientation analysis is performed on the Stereonet software (Allmendinger et al., 2011; Cardozo  
164 and Allmendinger, 2013). The spacing was analyzed by measuring the mean distance between plane  
165 traces belonging to the same set on an orthogonal plan.

166 Chromite distribution provides a guide for identifying the traces of the magmatic beddings (Leblanc,  
167 1980). Indeed, since chromite minerals are much denser than the matrix mainly consisting of Mg-rich  
168 silicates, they are easily visible by tomography. Thus, point clouds of chromite minerals are extracted  
169 from CT scans by using FIJI. Then the normal for each point is calculated before adjusting a plane for  
170 each chromite alignment. Orientation of the magmatic foliation is then derived from the plane  
171 orientation.

## 172 Fractal dimension analysis

173 Fractal dimension is an excellent tool to assess whether structures are statistically similar at different  
174 scales and characterize natural fracture networks (Basirat et al., 2019). Indeed, similar discontinuities  
175 have the same fractal dimension, whatever the scale. The fractal dimension of the fracture network is  
176 calculated on both the core sample and S\_2 to evaluate the self-similar character of fracture patterns  
177 at the cm-scale and mm-scale. Since Ni is denser than Mg and Si, Ni is an excellent signal to discriminate

178 mineralized fractures from the matrix. Thus, the micro-XRF Ni distribution map of the core sample was  
179 used to calculate the fractal dimension of the fracture network at the cm scale. Regarding the mm-  
180 scale, the S\_2 CT scan was selected because of the excellent density contrast observed between the  
181 fracture network and the matrix, which eases the extraction of the fracture network. Additional  
182 information on CT acquisition, structural features (fractures and chromite beddings) extraction and the  
183 fractal dimension analysis are given in Appendix A.

184

## 185 II.II. Petrophysical characterization.

### 186 Poro-permeability profile acquisition

187 Under weathering conditions, the hydrolysis of peridotites leads to the leaching of Mg and Si, causing  
188 an increase in the porosity (Butt and Cluzel, 2013). Furthermore, previous hydrological studies at the  
189 massif scale report changes in porosity and permeability with weathering stages in laterite profiles  
190 (Jeanpert, 2017; Join et al., 2005). Thus, a porosity-permeability profile is acquired along the core  
191 sample to describe better and characterize the weathering front in the sample. From the primary core  
192 sample, gas permeability was estimated on the five sub-samples, S\_3, S\_4, S\_5, S\_6 and S\_7, the others  
193 being impregnated with resin for the micro-XRF mapping. For each sample, 2 to 3 different  
194 permeability measures were carried out with a confining pressure of 120 bar and injection pressure  
195 varying from 50 bar to 80 bar in the triaxial cell. Injection pressure and injection volumes were  
196 measured over time to estimate the mass flux and thus the permeability  $k$  with Darcy's law.

197 The final permeability value corresponds to the mean value of the different measures for each sub-  
198 sample. Total water porosity was also estimated on the same sub-samples by measuring the weight  
199 and volume differences of dry and wet samples.

200 Based on the values obtained for these sub-samples and the mean X-ray attenuation profile from the  
201 tomographic acquisition of the main core sample, semi-quantitative water porosity and permeability  
202 profiles were obtained on the whole sample by interpolating the different values along the vertical.

203 This interpolation was based on the linear regression between the porosity and the mean attenuation  
204 displayed by the grey-scale pixel intensity values of the subsamples. A similar approach was then  
205 applied to the permeability. The linear regression equation should be taken carefully since only 5  
206 points were used to estimate it, thus providing a qualitative estimation of porosity and permeability  
207 profiles.

## 208 Pore size distribution

209 Mercury injection porosimetry was performed in the pressure range from 8.4 kPa to 413 MPa,  
210 corresponding to pore sizes from 88  $\mu\text{m}$  to 1.8 nm. This technique analyses the macro and mesopores  
211 and the pore size distribution. Sub-samples S\_3, S\_4, S\_5, S\_6 and S\_7 were analyzed.

212

## 213 II.III. Element distribution

### 214 $\mu$ -XRF element mapping

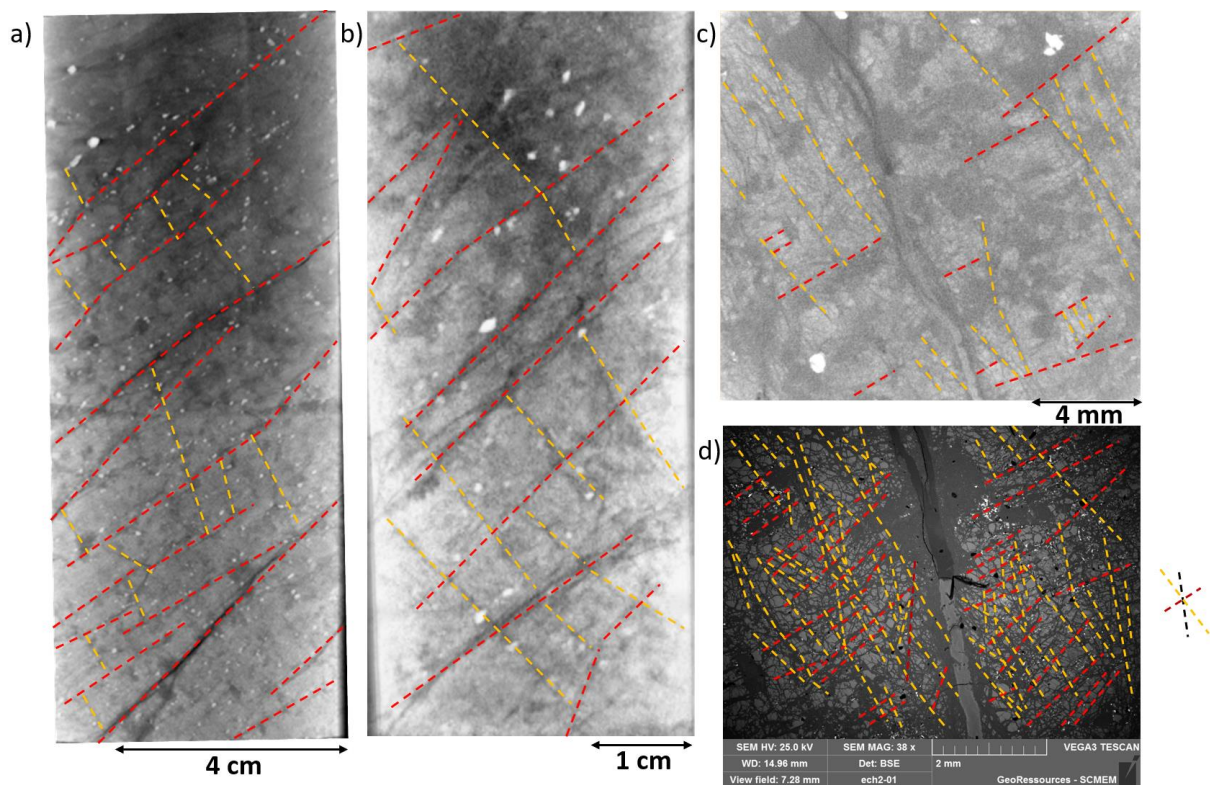
215 Chemical maps were acquired with an M4-Tornado Bruker micro-X-ray fluorescence spectrometer ( $\mu$ -  
216 XRF). A voltage of 50 kV and a current of 400  $\mu\text{A}$  with an acquisition time of 15 ms/pixel and spacing of  
217 100  $\mu\text{m}$  for the core sample and a spacing of 20  $\mu\text{m}$  for the S\_0 sub-zone and the S\_1 and S\_2 sub-  
218 samples were chosen to capture the signal of both heavy elements (Co, Ni, Fe, Cr) and light ones (Mg,  
219 Si). Semi-quantitative analysis was carried out to assess the concentration of the different elements  
220 for each map using the built-in, standardless quantification functionality of the software, which is  
221 based on Fundamental Parameter analysis. In addition, a semi-quantitative 300-point line was  
222 acquired to study the evolution of Ni, Mg, Fe and Si concentrations along the core sample. The chemical  
223 profile is compared with a geochemical log carried out along a drill core located 44 m away from the  
224 studied core sample in the Cagou Pit (latitude: 20°58'23.795" S, longitude: 164°47'29.732" E, altitude:  
225 730m).

226 III. Results

227 III.I. Structural organization

228 III.I.I. Fracture network description

229 Poorly mineralized serpentine-bearing fractures occur as low-density objects, appearing thus as dark  
230 grey structural elements on tomographic images. They are denser than the olivine- and  
231 orthopyroxene-rich matrix when containing high Ni amounts (Figure 3). The S\_2 CT image displays the  
232 clear transition between the two fracture types: the lower part of the primary fracture crossing the  
233 sample is light grey, thus denser than its upper part, which appears in dark grey (Figure 3.c). This  
234 transition is also well visible in the BSE imaging of sample S\_2 (Figure 3.d). In both cases, the contrast  
235 between the matrix and the fractures enables the discrimination of two distinct fracture sets (F1 set in  
236 red and F2 in yellow), whatever the scale (Figure 3). Chromites appear as intense white specks  
237 corresponding as they have the highest density (Figure 3).



238

239 Figure 3 - CT scans exhibiting two fracture sets highlighted by red (F1) and yellow (F2) dotted lines. a) Sample A. b) Sample

240

S\_0. c) S\_2 d) BSE imaging of S\_2

241

242 Data extraction as fractures from the CT has been applied on both core and S\_2 samples (Figure 4).

243 The samples are presented with the same orientation and display similar structural organization as

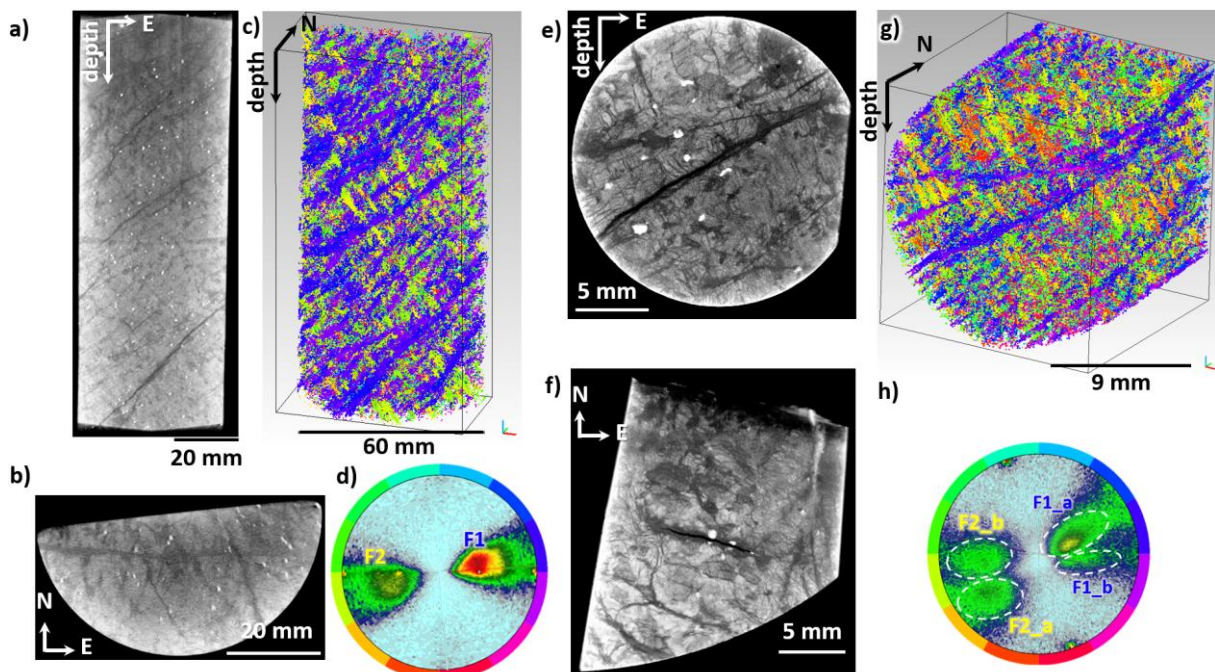
244 shown by the dip direction stereonet (Figure 4.d, Figure 4.h). The main microfracture set, F1 (dark blue

245 in Figure 4.c, Figure 4.g), is present in both samples. The second microfracture set, F2, is less well visible

246 in yellow. The mean poles (trend, plunge) are N80E,42 for F1 and N259E,34 for F2 in the core sample.

247 In S\_2, the mean pole of F1 is N70E,41 and N249E49 for F2. However, the F2 set is composite and

248 contains 2 sub poles families F2\_a and F2\_b.



249

250 *Figure 4 - Fracture extraction of core sample and sub-sample S\_2. a) & b) CT scans of core sample. c) Oriented point cloud*

251 *colored by dip direction. d) Stereographic projections of fracture orientations in the core sample (poles). e) & f) CT scans of*

252 *sub-sample S\_2. g) Oriented point cloud colored by dip direction. h) Stereographic projections of fracture orientations*

253 *(poles) of sub-sample S\_2 (poles).*

254 The microstructures in S\_2 are very similar to those of the core sample, with F1 sub-orthogonal to F2.

255 Planes were adjusted on data from each structural set (Figure 5.a, Figure 5.b, Figure 5.e). The relative

256 angle between the mean F1 set (N82E, 46) and F2 set (N254E, 40) planes is estimated at  $90\pm 4^\circ$  for the

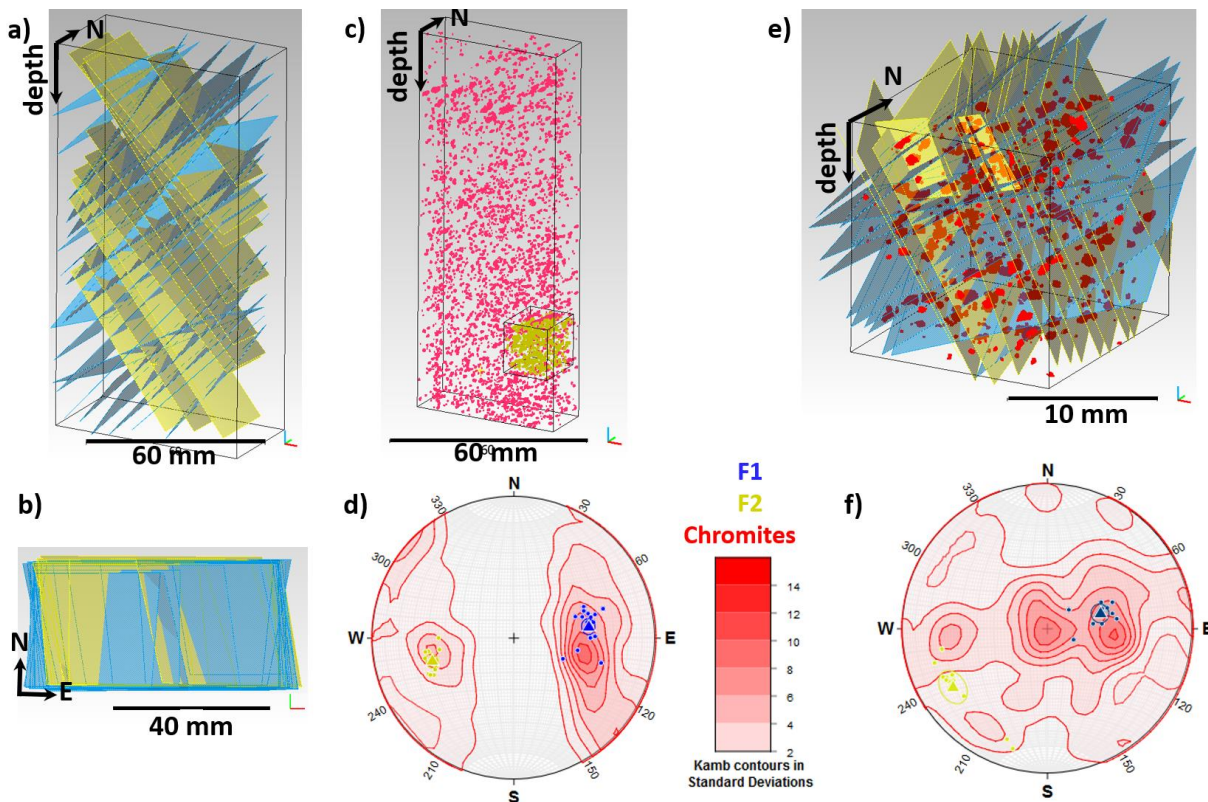
257 core sample, which confirms the orthogonality of the sets (Figure 5.d). On a smaller scale, in S\_2, an  
258 angle of  $90\pm 6^\circ$  between F1 (N74E,60) and F2 (N238E,24) was found (Figure 5.f).

259 The mean spacing for each set has been estimated from the spatial distribution of the adjusted planes.  
260 F1 has a denser distribution than F2 in the core sample with a mean spacing of  $4.8 \pm 0.5$  mm, while F2  
261 is characterized by a mean spacing of  $6.4 \pm 0.8$  mm with a 95% confidence interval. In S\_2, F1 and F2  
262 present a similar spatial distribution with a mean spacing of  $1.2 \pm 0.3$  mm for F1 and  $1.4 \pm 0.2$  mm for  
263 F2. Furthermore, scale invariance in the structural networks is confirmed by calculating the fractal  
264 dimension of networks: 1.79 for the core sample and 1.83 for sample S\_2.

265

### 266 III.1.II Magmatic foliation analysis

267 The orientation of the magmatic foliation, restored through the analysis of the distribution of chromite  
268 grains, was estimated and compared to fracture sets F1 and F2 (Figure 5). Despite a significant  
269 scattering of the magmatic foliation orientations in the core sample, they are better aligned with F1  
270 and subsequently orthogonal to F2 (Figure 5.c, Figure 5.d). Indeed, the Kamb contour points out the  
271 significant clusters in the poles distribution of the chromite alignments (Kamb, 1959). Thus, the slight  
272 angle deviation between the F1 mean pole and the center of the highest Kamb contour, estimated at  
273  $0\pm 14^\circ$ , supports the alignment of F1 with the magmatic foliation. This result is also found at a smaller  
274 scale in sample S\_2 (Figure 5.e, Figure 5.f).



275

276

277

278

279

280

281

Figure 5 – Comparison of structural sets with chromite grains alignment. a) 3D view of adjusted planes to F1 (blue) and F2 (yellow) of the core sample. b) North view of adjusted planes to F1 (blue) and F2 (yellow) of the core sample. c) Distribution of the chromites (in red) in the core sample and localization of the sub-sample S2 (yellow). d) Pole distribution of F1 (blue), F2 (yellow) with their mean vectors, and contour plot of chromites alignment (red) of the core sample. e) 3D view of adjusted planes to F1 (blue), F2 (yellow) and chromites distribution (red) in S\_2. f) Pole distribution of F1 (blue), F2 (yellow) with their mean vectors, and contour plot of chromites alignment (red) of S\_2.

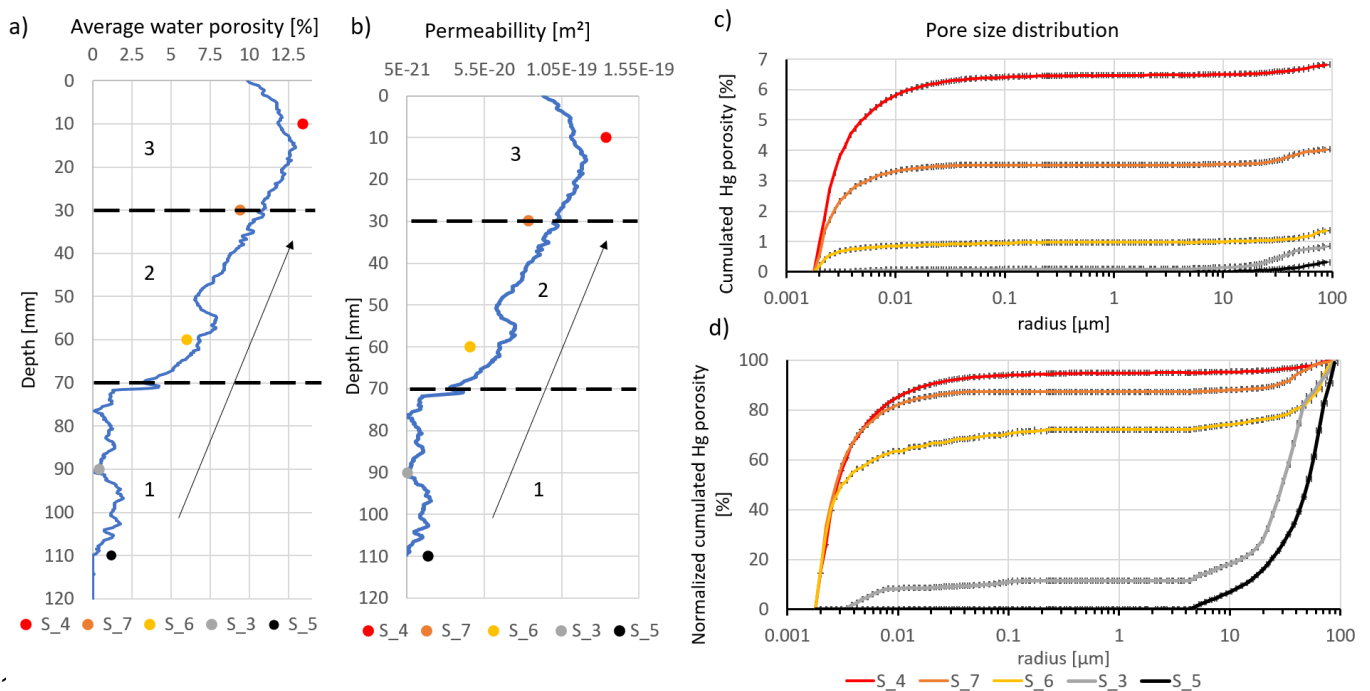
### 282 III.II Poro-permeability characterization

283 The gas permeability and total water porosity along the longitudinal axis of the core increase upwards  
 284 along with weathering intensity. Three different zones can be outlined (Figure 6.a,b): i) a first one  
 285 defined by low porosity (< 2.5%) and low permeability (< 1E-20 m<sup>2</sup>), ii) a transition zone then occurs  
 286 where porosity increases from 3% to 12%, while the permeability increases from 1E-20 m<sup>2</sup> to more  
 287 than 1E-19 m<sup>2</sup>, iii) in the most weathered portion of the core sample, the porosity is relatively constant  
 288 at about 13%, while permeability is about 1.2E-19 m<sup>2</sup>.

289 Mercury porosimetry confirms the observed trends (Figure 6.c, d). The bottom of the core sample is  
 290 characterized by low porosity (< 1%), while the top exhibits a higher porosity (> 7%). Furthermore, the

291 change in pore size distribution reveals that the increase in porosity results from the opening of  
 292 nanometer pores (< 50 nm). The connected porosity of the weathered part of the core sample (samples  
 293 S\_4 and S\_7) is characterized at 90% by nanopores with sizes ranging from 1.8 nm to 30 nm and a  
 294 minor (10%) family of micropores with sizes ranging from 4  $\mu\text{m}$  to 80  $\mu\text{m}$ . Conversely, the fresh part  
 295 of the core sample (S\_3 and S\_5) is characterized by micropores ranging from 4  $\mu\text{m}$  to 80  $\mu\text{m}$ ,  
 296 accounting for 90% to 100% of the effective porosity. The minor family of nanopores, with sizes ranging  
 297 from 1.8 nm to 30 nm, accounts for 0% to 10% of the porosity for S\_3 and S\_4. The sub-sample S\_6  
 298 presents intermediate features with 70% of the porosity due to nanopores and 30% to micropores  
 299 (Figure 6.d)

300



301

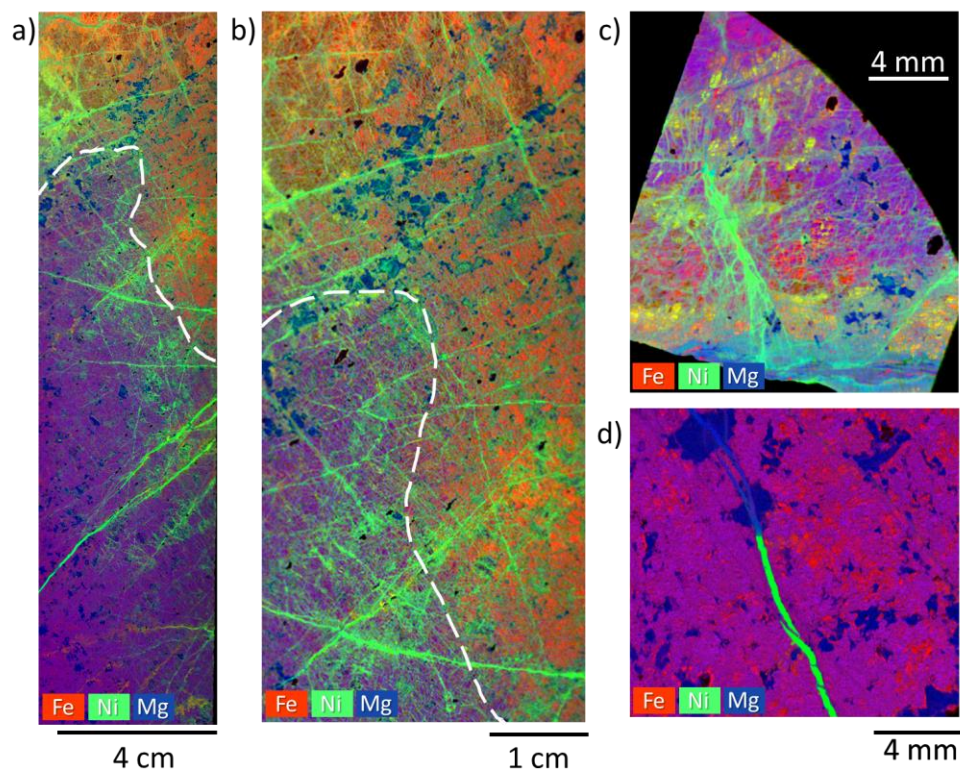
302 *Figure 6 - Total water porosity and permeability distribution in the core sample. a) Total water porosity. The plotted points*  
 303 *represent the measured porosity, while the curve results from the linear regression between the measured porosity and the*  
 304 *mean greyscale intensity value. b) Permeability. The plotted points represent the measured permeability, while the curve*  
 305 *results from the linear regression between the measured permeability and the mean greyscale intensity value. c) Pore size*  
 306 *distribution based on cumulated Hg porosity. d) Pore size distribution based on normalized cumulated Hg porosity*

307

### 308 III.III. Element redistribution

#### 309 III.III. I. Element mapping

310 The Fe, Ni, and Mg XRF maps provide a good image of the microfracture network and their infillings at  
311 different scales. Ni is mainly present in fractures at each scale, while Si, Mg, and Fe dominate within  
312 the matrix (Figure 7). Two distinct areas can be distinguished (Figure 7.a, Figure 7.b). The saprock zone  
313 exhibits an enrichment in Fe at the expense of Mg compared to the least weathered portion located  
314 below the line. In addition, the apparent density of Ni-bearing fractures is higher in the saprock (Figure  
315 7.a, Figure 7.b). In the map obtained on S\_1, located in the most weathered part of the ore sample, Ni  
316 occurs in both major and secondary fracture networks (Figure 7.c). On the contrary, the map obtained  
317 on S\_2, located in the least weathered part of the core sample, shows that Ni is solely present within  
318 the major fracture (Figure 7.d).

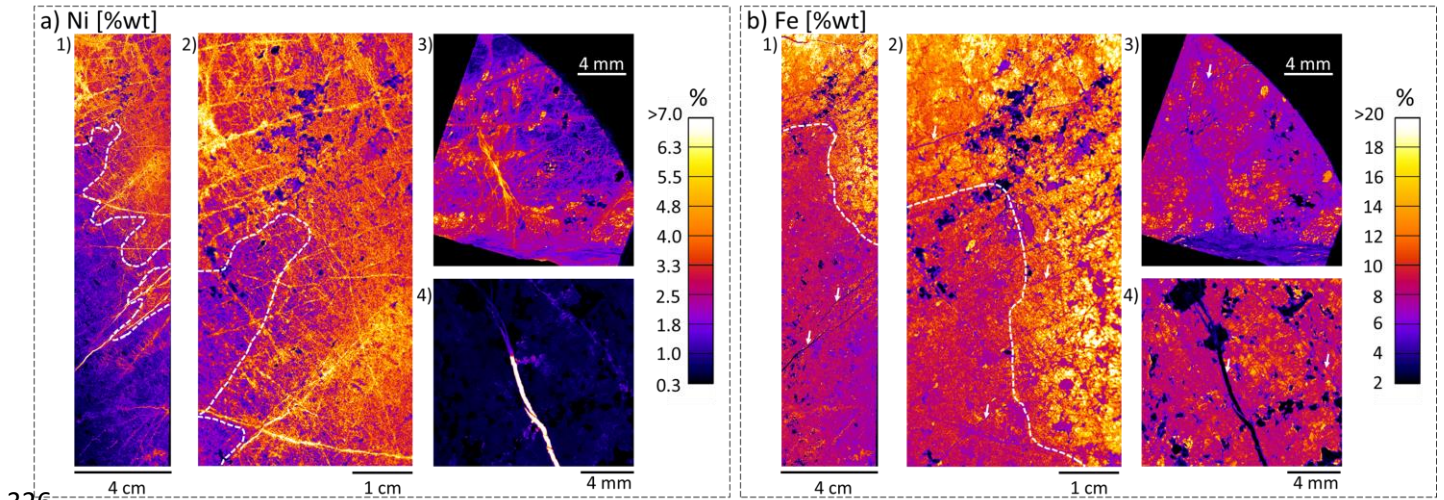


319

320 *Figure 7 – RGB composite map of Fe-Ni-Mg distributions in a) Core sample. b) Sample S\_0. c) Sample S\_1. d) Sample S\_2*

321 The semi-quantitative Ni and Fe chemical maps support previous observations: Ni is mainly located in  
322 fractures where grades vary from ca. 5 to > 9 wt% (Figure 8). In the weathered part, the matrix is richer

323 in Ni (grades up to ca. 3 wt%). On the contrary, the Ni content drops from ca. 2 wt% Ni near the line to  
 324 1 wt% Ni in the freshest part of the sample (Figure 8.a.1, Figure 8.a.2). In sample S\_2, the matrix is Ni  
 325 poor with values close to the fresh rock (Figure 8.a.4).



326  
 327 *Figure 8- Semi-quantitative concentration maps of a) Ni of 1. Core Sample. 2. Sample S\_0. 3. Sample S\_1. 4. Sample S\_2.*  
 328 *and of b) Fe of 1. Core Sample. 2. Sample S\_0. 3. Sample S\_1. 4. Sample S\_2.*

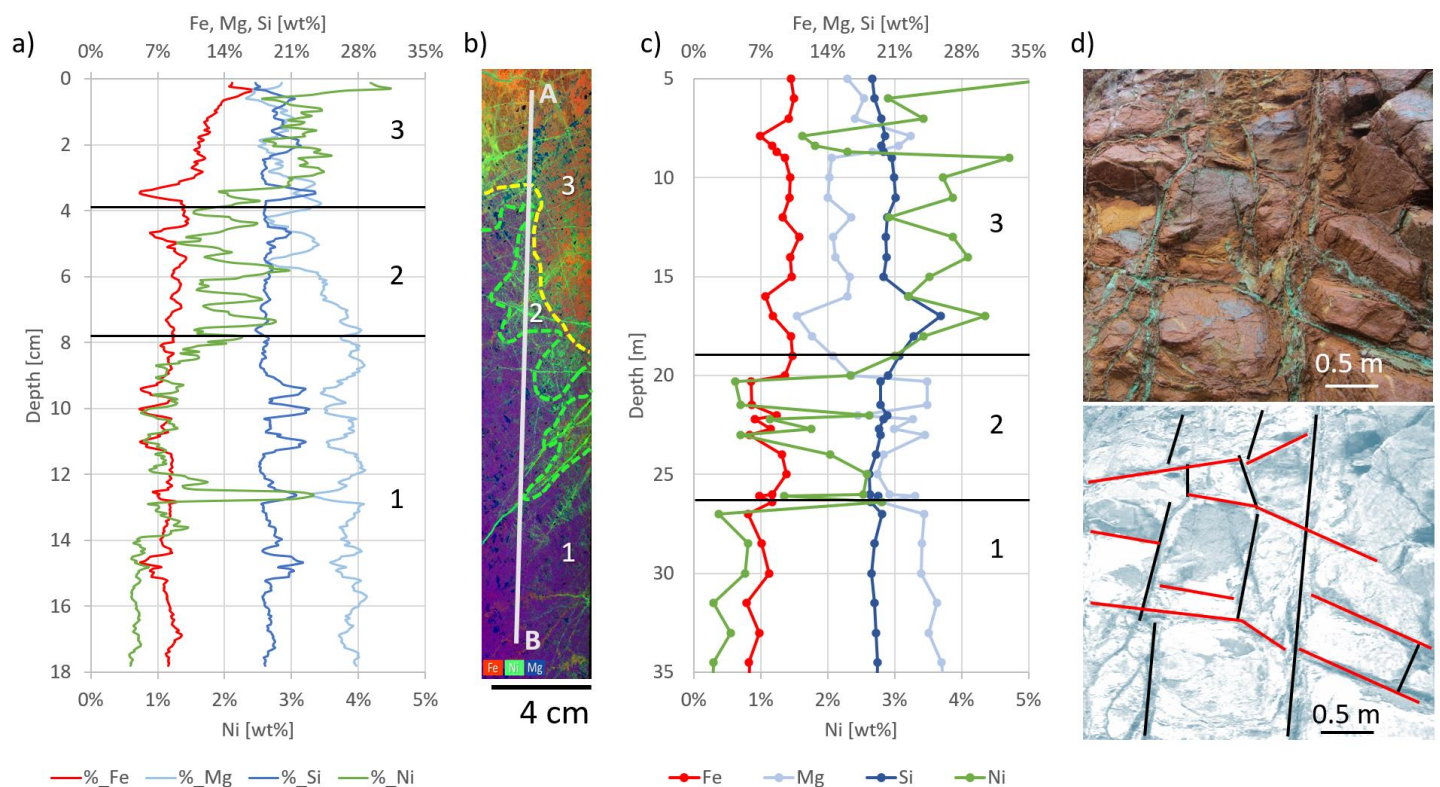
329 The Fe-map also displays two chemical domains for the core sample and sample S\_2 (Figure 8.b). The  
 330 Fe-rich region occurs in the uppermost part of the core sample, closer to the top than the Ni-rich area  
 331 (Figure 8.b.1, Figure 8.b.2). Fe content exceeds the 10 wt% in the weathered area and remains close  
 332 to 8 wt% in fresher rock. Fractures are free of Fe, as underlined by the white arrows.

### 333 III.III. II. Chemical profiles

334 The Ni, Fe, Mg, and Si chemical transect across the core sample reveals the geochemical impact of  
 335 weathering at the cm-scale (Figure 9.a, Figure 9.b). To draw comparisons with systems at a larger scale,  
 336 we report a geochemical log carried out along a drill core located in Cagou Pit (Figure 9.c). From the  
 337 least to most weathered part of the core sample (i.e. from bottom to top), Fe and Ni concentrations  
 338 increase at the expense of Mg, while Si remains constant (Figure 9.a). Three different zones are thus  
 339 distinguished in the profile. The first one is characterized by low Ni (0.5 wt% - 1 wt%) and Fe (7 wt%)  
 340 concentrations and high Mg (27 wt%) and Si (20 wt%) concentrations. The second zone exhibits an  
 341 increase in Ni up to 2 wt%, Fe up to 9 – 10 wt%, and Mg decrease to 20 wt%. The third zone is associated

342 with a sharp rise of Ni and Fe contents up to 3 wt% and 15 wt%, respectively, while the Mg content  
 343 remains around 20 wt%. Whereas the broader trends represent the evolution of the matrix  
 344 composition, Ni spikes result from microfractures. The analysis of the Ni signal in the transition zone  
 345 using a Fast Fourier Transform reveals a periodicity of the spikes of 7 mm, similar to the estimated  
 346 spacing of F1 (5 mm) and F2 (6 mm) in the core sample.

347 At a larger scale, the 30 m-long drill core crosses from bottom to top, i) peridotite rock (up to 26 m), ii)  
 348 earthy saprolite interlayered with slightly weathered rock (from 26 m to 19 m), and (iii) earthy saprolite  
 349 (up to 5 m). The drill core exhibits geochemical trends similar to those observed within the 30 cm-long  
 350 core sample (Figure 9.c). Specifically, from bottom to top, Fe and Ni concentrations increase at the  
 351 expense of Mg, while Si remains constant at about 20 wt%. Furthermore, the three geochemical zones  
 352 identified in the core sample are expressed at a larger scale along with the entire drill core.



354 *Figure 9 – a) Semi-quantitative Ni, Fe, Mg, Si profile in wt% along with the core sample. b) RGB composite map of Fe-Ni-Mg*  
 355 *in the core sample, defining three distinct geochemical zones – 1: Poorly weathered area – 2: Transition area – 3: Weathered*  
 356 *area. c) Geochemical log (Ni, Fe, Si, Mg in wt%) of a drill core. d) Ni-rich fracture network (green filling) at the outcrop scale.*  
 357 *Two sub-orthogonal fracture sets are observed: F1 (black) and F2 (red).*

## 358 IV. Discussion

359

### 360 IV.I. Weathering rate along the penetrating alteration front

361

362 The evolution of whole-rock density, porosity and permeability in the core sample corresponds to a  
363 petrophysical and chemical gradient from the quasi-fresh facies at the bottom to an advanced  
364 alteration state at the top. The main feature is a density decrease correlated to porosity increase. The  
365 measured petrophysical properties of the fresh rock (i.e., low porosity of ~1% and very low  
366 permeability  $< 1E-20 \text{ m}^2$ ) are similar to those obtained on fresh Oman harzburgites (Dewandel et al.,  
367 2005; Katayama et al., 2020). Both peridotites are comparable in terms of chemistry and mineralogy  
368 (Al-Khribash, 2015). Therefore, the properties of both Oman and New Caledonia ophiolite aquifers  
369 would be similar (Dewandel et al., 2017; Jeanpert, 2017).

370 The chemical evolution at the core sample scale is similar to that at the outcrop scale  
371 (Cathelineau et al., 2017; Muñoz et al., 2019; Teitler et al., 2019). As attested by high Mg and Si bulk  
372 contents, the olivine remains preserved from dissolution in the fresh facies. Ni is locally present in the  
373 prominent fractures as newly-formed phyllosilicates within an almost unaltered matrix. The newly-  
374 formed phyllosilicates correspond to Mg-Ni talc-like, as already observed in previous studies from the  
375 same area (Cathelineau et al., 2017, 2016; Muñoz et al., 2019). In the weathering front, the porosity  
376 and permeability increase with nanoporosity development. Mg and Si remain elevated, while Ni and  
377 Fe start to increase. Ni enrichments correspond to the two sub-orthogonal microfracture sets, e.g. F1  
378 and F2. The FFT analysis from the Ni profile (zone (2)) reveals a spatial periodicity of 7 mm, which is  
379 close to the mean spacing of F1: 5 mm and F2: 6 mm. When weathering progresses, olivine dissolves  
380 and the bulk Fe and Ni content increase significantly while Mg decreases. Fe precipitates as goethite  
381 and serpentine (mostly lizardite) remains preserved (Myagkiy et al., 2017; Teitler et al., 2019). Ni

382 enrichment mainly occurs in the fractures and within the micro-fractured matrix in the altered zone.  
383 At this weathering stage, the porosity is relatively high (around 10%), and the nanopores account for  
384 almost all the connected porosity.

#### 385 IV.II. Element redistribution on fractures network

386

387 The distribution of three different weathering rates in the core sample results from several processes  
388 that are not all synchronous (Figure 9.b). When the olivine dissolution front progresses downwards, a  
389 part of magnesium and nickel is trapped by the precipitation of phyllosilicates such as Mg-Ni talc-like  
390 (Cathelineau et al., 2017, 2016; Myagkiy et al., 2017). These secondary minerals are richer in Si and Ni  
391 and poorer in Mg than the original silicates, explaining thus the enrichments. The precipitation of Fe-  
392 oxy-hydroxides fixes iron ( $\text{Fe}^{3+}$ ). Ni excess migrates following the fracture network towards deeper,  
393 poorly weathered levels. This migration ahead of the dissolution front saturates fractures, creating the  
394 transition area observed in the core sample. Ni enrichment occurs mainly in the vicinity of the main  
395 microfractures, within the dense network of serpentine microcracks that forms the so-called “mesh”  
396 structure (Cathelineau et al., 2017; Muñoz et al., 2019). In this area, silicates are mostly un-weathered.  
397 The dissolution-precipitation process triggers the bulk permeability increase with the nanopore  
398 formation. Thus, a transition occurs from diffusion- to advection-driven reaction front at the sub-mm  
399 scale. The nanopores are probably controlled by the distribution of serpentine and its nano-defects.  
400 Therefore, in increasingly serpentinized rocks, the nano-defects may affect the distribution of  
401 nanopores (Tutolo et al., 2016). Dewandel et al. (2005) also reported a similar pore size distribution on  
402 fresh peridotites from Oman and interpreted it related to the serpentine vein microstructures. Our  
403 data indicate that the weathering processes can also contribute to the nanoporosity formation in  
404 serpentinized peridotite. Inherited nano defects may probably explain the enhanced nanoporosity  
405 development. In addition, the supergene weathering of the serpentine and the opening of inherited

406 serpentine microfracture and their infilling by newly formed phyllosilicates both impact the pore size  
407 distribution. The dissolution front favors the onset of nanopores, which extends it to the whole sample.  
408 This redistribution model highlights the impact of pre-existing fracture networks, which act as  
409 preferential pathways for the Ni-Mg-Si transfers and their reprecipitation as newly formed minerals.

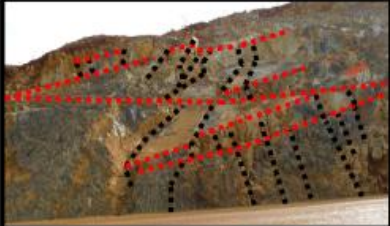
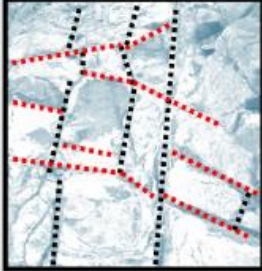
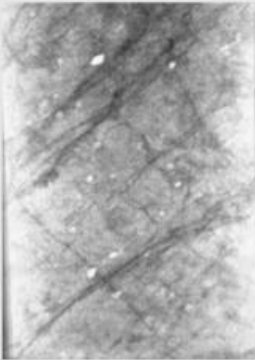
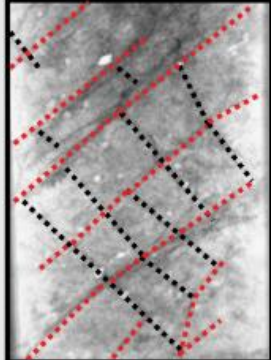
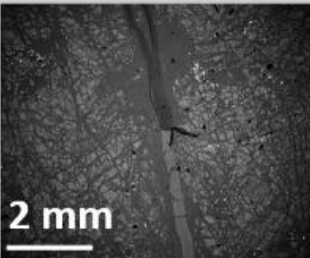
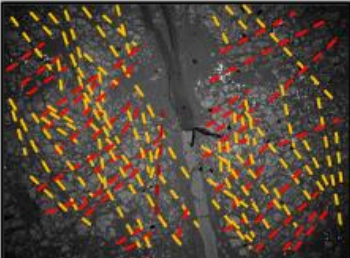
410

#### 411 IV.III. Multiscale redistribution processes

412

413 The structural organization of the fracture network and the chromite layering of both core sample and  
414 sample S\_2 exhibits a predominant fracture set (F1) parallel to the chromite alignments and a second  
415 set (F2) sub-orthogonal to F1. Previous studies have highlighted the link between chromite layering  
416 and magmatic foliation (Cassard et al., 1981; Cluzel et al., 2012; Prinzhofer et al., 1980) and have  
417 suggested an N-S striking orientation for such lineation (Cluzel et al., 2012). Furthermore, this lineation  
418 would be relicts of the oceanic lithosphere (Cluzel et al., 2012). Thus, a geometric link between the  
419 fracture network and the magmatic bedding could be inferred, with F1 oriented parallel to the  
420 magmatic lineation and F2 orthogonal to such orientation. Besides, recent studies point out that  
421 fractures filled by primary serpentine (lizardite) are also inherited from relicts of the oceanic  
422 lithosphere (Cathelineau et al., 2017; Iseppi et al., 2018; Quesnel et al., 2016). In addition, such an  
423 inherited fracture network often displays sub-orthogonal sets of fractures striking N0-20°E, N50-70°E,  
424 N90-100°E and N120-140°E with variable dips from 20 to 90° (Iseppi, 2018; Iseppi et al., 2018). Such a  
425 common origin of the magmatic lineation and the inherited fracture network, combined with a similar  
426 orientation between such structures, may allow suggesting an orientation of the fracture network in  
427 the core sample close to what has been described by Iseppi et al. (2018). A similar structural  
428 organization occurs on larger scales (Figure 10). Sub-orthogonal fracture sets from the Cagou and the  
429 Test pit (Figure 1.b) are described from mm to 10 m scale. At the outcrop scale (1m to 10m),  
430 Cathelineau et al. (2016) also describe sub-orthogonal structures for Ni talc-like crack-seal fractures

431 with two strike families of N150° and N50° at the Cagou pit. At the massif scale , such as the example  
432 of Koniambo, four dominant fracture sets strike N0°, N45°, N90° and N135° (Jeanpert et al., 2019;  
433 Quesnel et al., 2016). The serpentine fracture network is characterized by an N130° dominant trend  
434 associated with N90°, N45° and N0° directions (Iseppi et al., 2018). This general structural organization  
435 at the island scale shows two different sets of two sub-orthogonal families (N0° associated with N90°  
436 and N45° associated with N130°). Thus, it is proposed that a specific structural organization including  
437 one to two sub orthogonal sets of fracture striking N0° – N90° and N45° – N135° would be developed  
438 at different scales, which suggests that similar structural processes would have occurred to constrain  
439 the system. A fractal dimension estimated on the core sample and the sub-sample S\_2 can be proposed  
440 at around 1.8 to quantify the self-similarity of the fracture network.

Scale	Image	Interpretation	Permeability [ $m^2$ ]
10 m			$1e-13 m^2$ (Jeanpert 2017)
1 m			$1e-14 m^2$ (Jeanpert 2017)
10 cm			$1e-15 m^2$ (Jeanpert et al 2019) - $1e-16 m^2$ Dewandel et al 2005)
1 cm			$1e-16 m^2$ (Dewandel et al 2005)
1 mm			$1e-21 - 1e-19 m^2$

441

442 *Figure 10 - Multiscale image panel of fracture networks. The images are coming from samples located in Cagou and the Test*

443 *pit (Fig1.b). On the interpreted images, two sub orthogonal sets are observed: F1 (black and yellow) and*

444 *F2 (red)*

445 (Jeanpert et al., 2019) have already pointed out the relationship between fracture distribution and  
446 permeability at the outcrop scale. Our core-scale analysis supports this scaling effect on permeability.  
447 At the decimeter scale, the permeability of a fresh peridotite is estimated around  $1e-15 \text{ m}^2$ . Such value  
448 is far higher than the measured permeability in the core sample, i.e. between  $1e-21 \text{ m}^2$  and  $1e-19 \text{ m}^2$ .  
449 Instead, such permeability would result from fractures with a spacing of 0.35 m (Figure 10), yielding  
450 an aperture of  $1.6e-5 \text{ m}$  using a cubic law (Jeanpert, 2017). Similarly, at the 10 m scale, the permeability  
451 increases up to  $1e-13 \text{ m}^2 - 1e-11 \text{ m}^2$ , which is interpreted as draining fractures with a spacing of 30 m  
452 and an aperture of  $1.5e-3 \text{ m}$ , consistent with in situ observations (Figure 10).

453 This self-similarity in the structural organization at the different scales is also observed in the different  
454 weathering stages. Specifically, at the sample scale, this study highlights that the progression of the  
455 silicate dissolution front through a fracture network results in the redistribution of Ni and the  
456 development of different weathering facies within a few tens of centimetres. Such a gradation of the  
457 weathering products is also observed at the outcrop scale. The base of the lateritic profile usually  
458 includes a transition domain, up to a few meters in thickness, where Ni-rich fractures crosscut the  
459 unaltered bedrock. Upwards, this transition domain is delimited by the silicate dissolution front. In the  
460 saprolite above the front, secondary phyllosilicates formed away from the primary mineralized  
461 fractures (Cathelineau et al., 2016). The chemical (this study) and mineralogical (previous studies at  
462 the same location: Cathelineau et al. (2017, 2016); Muñoz et al. (2019); Teitler et al. (2019)) evolutions  
463 observed in lateritic profiles mimic, at a larger scale, the cm-scale processes observed in the core  
464 sample. In particular, the Ni distribution between the fractures and the saprolite matrix is similar at  
465 both scales. Thus, an average Ni grade in the saprolite ore is about 2-5 wt% (Butt and Cluzel, 2013),  
466 while Mg-Ni talc-like veins grade over 10 wt% (Cathelineau et al., 2017).

467 The chemical profile acquired on the core sample can thus be compared with drill core assay data  
468 (Figure 9). Indeed, when the log presents a continuous weathering process, the geochemical trends  
469 observed at the scale of a few decimeters are similar to those found commonly in the saprolite zone

470 of ultramafic-derived lateritic profiles (Teitler et al., 2019) (Figure 9.b). Such structural, weathering and  
471 geochemical similarities observed from 1e-3 m to 10 m scale highlight the impact of fractures network  
472 on weathering and redistribution processes at each observation scale. Hence a better understanding  
473 of the structural organization of the sample could provide light on the spatial geochemical distribution.

## 474 V. Conclusion

475 This study presents a multiscale approach combining structural, petrophysical, and geochemical  
476 analysis. The goal was to study the impact of the structural organization on the weathering processes  
477 and the Ni redistribution at different scales to discuss the similarities. Observation conducted at a small  
478 scale gives insight into the general mechanisms typical of the whole lateritic profiles. The main findings  
479 are:

- 480 - Weathering and Ni-enrichment are fracture controlled. The magmatic foliation guided the  
481 development of the serpentine networks, which constitute the active network favoring the  
482 penetration of meteoric waters. The main tectonics lineations observed in the Cagou sample  
483 and at the scale of Koniambo massif are NS, EW, NWSE, and SWNE. Microfracture sets are  
484 organized similarly at the sample scale and the open pit scale or even larger scale. This scale  
485 invariance suggests a common origin of the fracture networks, confirmed by their similar  
486 serpentine infillings and fractal distribution.
- 487 - The proposed multi-step Ni-redistribution at the core scale is consistent with existing chemical  
488 profiles in laterites. Fractures constitute sites of early fixation of Ni as newly-formed Mg-Ni-  
489 phyllosilicates. The reactivated serpentine microfractures are the primary enrichment locus  
490 before a bulk nickel redistribution by the dissolution front.
- 491 - The increase in porosity results from several superimposed processes: i) mesopore formation  
492 through olivine dissolution, ii) partial to full infilling of the pores by newly formed minerals  
493 such as neo-formed phyllosilicates and smectite described in previous works (Muñoz et al.,  
494 2019; Teitler et al., 2019). The newly formed phases display a remarkable high content of

495 nanopores. Further studies will be needed to determine the increase of the nanoporosity as it  
496 may affect the redistribution processes at a microscopic scale by favoring diffusion over  
497 advection.

498 - The weathering fronts observed at a small scale on a core sample are excellent analogues of  
499 the larger scale laterite profiles. In such profiles, the inherited fracture networks filled by  
500 serpentine developed in earlier stages and depend on magmatic microtextures and  
501 subduction-obduction history. They constitute the Ni-trap and show fractal dimensions.

502 - The Ni-redistribution results from a hierarchical and multi-scale organization related to the  
503 previous deformation. The self-similarity of spatial distribution patterns implies scaling laws.  
504 The evaluation of upscaling laws would, in consequence, open up great opportunities for  
505 designing reliable large-scale model geometry and better predictive models of Ni-  
506 mineralization location.

## 507 Acknowledgements

508 This work has been funded and logistically supported by the CNRT research contract CSF N° 9PS2017-  
509 CNRT.GEORESSOURCE/TRANSNUM« Facteurs d'enrichissements et transferts de Ni, Co-Sc dans les  
510 saprolites de Nouvelle Calédonie : approche géométrique, minéralo-géochimique et numérique », and  
511 by the French National Research Agency through the national program "Investissements d'avenir" of  
512 the Labex Ressources 21 with the reference ANR-10-LABX-21-01/ LABEX RESSOURCES21. The authors  
513 would like to thank Dr. Andreï Lecomte and Dr. Christophe Morlot (GeoRessources, Vandœuvre-lès-  
514 Nancy, France) for technical support in providing analytical data, and the anonymous reviewers and  
515 Peter C. Lightfoot for their careful reading of the manuscript and their insightful comments and  
516 suggestions.

## 517 References

- 518 Afshari Moein, M.J., Valley, B., Evans, K.F., 2019. Scaling of Fracture Patterns in Three Deep  
519 Boreholes and Implications for Constraining Fractal Discrete Fracture Network Models. *Rock*  
520 *Mech. Rock Eng.* 52, 1723–1743. <https://doi.org/10.1007/s00603-019-1739-7>
- 521 Al-Khirbash, S., 2015. Genesis and mineralogical classification of Ni-laterites, Oman Mountains. *Ore*  
522 *Geol. Rev.* 65, 199–212. <https://doi.org/10.1016/j.oregeorev.2014.09.022>
- 523 Allègre, C.J., Le Mouel, J.L., Provost, A., 1982. Scaling rules in rock fracture and possible implications  
524 for earthquake prediction. *Nature* 297, 47–49. <https://doi.org/10.1038/297047a0>
- 525 Allmendinger, R.W., Cardozo, N., Fisher, D.M., 2011. *Structural Geology Algorithms: Vectors and*  
526 *Tensors*. Cambridge University Press, Cambridge.  
527 <https://doi.org/10.1017/CBO9780511920202>
- 528 Basirat, R., Goshtasbi, K., Ahmadi, M., 2019. Determination of the Fractal Dimension of the Fracture  
529 Network System Using Image Processing Technique. *Fractal Fract.* 3, 17.  
530 <https://doi.org/10.3390/fractalfract3020017>
- 531 Best, M.E., 2015. Mineral Resources, in: *Treatise on Geophysics*. Elsevier, pp. 525–556.  
532 <https://doi.org/10.1016/B978-0-444-53802-4.00200-1>
- 533 Bonnet, E., Bour, O., Odling, N.E., Davy, P., Main, I., Cowie, P., Berkowitz, B., 2001. Scaling of fracture  
534 systems in geological media. *Rev. Geophys.* 39, 347–383.  
535 <https://doi.org/10.1029/1999RG000074>
- 536 Boulch, A., Marlet, R., 2012. Fast and Robust Normal Estimation for Point Clouds with Sharp Features.  
537 *Comput. Graph. Forum* 31, 1765–1774. <https://doi.org/10.1111/j.1467-8659.2012.03181.x>
- 538 Bour, O., 2002. A statistical scaling model for fracture network geometry, with validation on a  
539 multiscale mapping of a joint network (Hornelen Basin, Norway). *J. Geophys. Res.* 107, 2113.  
540 <https://doi.org/10.1029/2001JB000176>

541 Butt, C.R.M., Cluzel, D., 2013. Nickel Laterite Ore Deposits: Weathered Serpentinites. *Elements* 9,  
542 123–128. <https://doi.org/10.2113/gselements.9.2.123>

543 Cardozo, N., Allmendinger, R.W., 2013. Spherical projections with OSXStereonet. *Comput. Geosci.* 51,  
544 193–205. <https://doi.org/10.1016/j.cageo.2012.07.021>

545 Cassard, D., Nicolas, A., Rabinovitch, M., Moutte, J., Leblanc, M., Prinzhofer, A., 1981. Structural  
546 classification of chromite pods in southern New Caledonia. *Econ. Geol.* 76, 805–831.  
547 <https://doi.org/10.2113/gsecongeo.76.4.805>

548 Cathelineau, M., Myagkiy, A., Quesnel, B., Boiron, M.-C., Gautier, P., Boulvais, P., Ulrich, M., Truche,  
549 L., Golfier, F., Drouillet, M., 2017. Multistage crack seal vein and hydrothermal Ni enrichment  
550 in serpentinitized ultramafic rocks (Koniambo massif, New Caledonia). *Miner. Deposita* 52,  
551 945–960. <https://doi.org/10.1007/s00126-016-0695-3>

552 Cathelineau, M., Quesnel, B., Gautier, P., Boulvais, P., Couteau, C., Drouillet, M., 2016. Nickel  
553 dispersion and enrichment at the bottom of the regolith: formation of pimelite target-like  
554 ores in rock block joints (Koniambo Ni deposit, New Caledonia). *Miner. Deposita* 51, 271–  
555 282. <https://doi.org/10.1007/s00126-015-0607-y>

556 Chevillotte, V., 2005. Morphogenèse tropicale en contexte épirogénique modéré : exemple de la  
557 Nouvelle-Calédonie (Pacifique Sud-Ouest) (Theses). Université de la Nouvelle-Calédonie.

558 Cluzel, D., Aitchison, J.C., Picard, C., 2001. Tectonic accretion and underplating of mafic terranes in  
559 the Late Eocene intraoceanic fore-arc of New Caledonia (Southwest Pacific): geodynamic  
560 implications. *Tectonophysics* 340, 23–59. [https://doi.org/10.1016/S0040-1951\(01\)00148-2](https://doi.org/10.1016/S0040-1951(01)00148-2)

561 Cluzel, D., Maurizot, P., Collot, J., Sevin, B., 2012. An outline of the Geology of New Caledonia; from  
562 Permian-Mesozoic Southeast Gondwanaland active margin to Cenozoic obduction and  
563 supergene evolution. *Episodes* 35, 72–86.

564 de Dreuzy, J.-R., Méheust, Y., Pichot, G., 2012. Influence of fracture scale heterogeneity on the flow  
565 properties of three-dimensional discrete fracture networks (DFN): 3D FRACTURE NETWORK

566 PERMEABILITY. *J. Geophys. Res. Solid Earth* 117, n/a-n/a.  
567 <https://doi.org/10.1029/2012JB009461>

568 Dewandel, B., Jeanpert, J., Ladouche, B., Join, J.-L., Maréchal, J.-C., 2017. Inferring the heterogeneity,  
569 transmissivity and hydraulic conductivity of crystalline aquifers from a detailed water-table  
570 map. *J. Hydrol.* 550, 118–129. <https://doi.org/10.1016/j.jhydrol.2017.03.075>

571 Dewandel, B., Lachassagne, P., Boudier, F., Al-Hattali, S., Ladouche, B., Pinault, J.-L., Al-Suleimani, Z.,  
572 2005. A conceptual hydrogeological model of ophiolite hard-rock aquifers in Oman based on  
573 a multiscale and a multidisciplinary approach. *Hydrogeol. J.* 13, 708–726.  
574 <https://doi.org/10.1007/s10040-005-0449-2>

575 Dublet, G., Juillot, F., Morin, G., Fritsch, E., Fandeur, D., Brown, G.E., 2015. Goethite aging explains Ni  
576 depletion in upper units of ultramafic lateritic ores from New Caledonia. *Geochim.*  
577 *Cosmochim. Acta* 160, 1–15. <https://doi.org/10.1016/j.gca.2015.03.015>

578 Dublet, G., Juillot, F., Morin, G., Fritsch, E., Fandeur, D., Ona-Nguema, G., Brown, G.E., 2012. Ni  
579 speciation in a New Caledonian lateritic regolith: A quantitative X-ray absorption  
580 spectroscopy investigation. *Geochim. Cosmochim. Acta* 95, 119–133.  
581 <https://doi.org/10.1016/j.gca.2012.07.030>

582 Freyssinet, Ph., Butt, C.R.M., Morris, R.C., Piantone, P., 2005. Ore-Forming Processes Related to  
583 Lateritic Weathering, in: One Hundredth Anniversary Volume. Society of Economic  
584 Geologists. <https://doi.org/10.5382/AV100.21>

585 Fritsch, E., Juillot, F., Dublet, G., Fonteneau, L., Fandeur, D., Martin, E., Caner, L., Auzende, A.-L.,  
586 Grauby, O., Beaufort, D., 2016. An alternative model for the formation of hydrous Mg/Ni  
587 layer silicates ('deweylite'/'garnierite') in faulted peridotites of New Caledonia: I. Texture and  
588 mineralogy of a paragenetic succession of silicate infillings. *Eur. J. Mineral.* 28, 295–311.  
589 <https://doi.org/10.1127/ejm/2015/0027-2503>

590 Fu, W., Zhang, Y., Pang, C., Zeng, X., Huang, X., Yang, M., Shao, Y., Lin, H., 2018. Garnierite  
591 mineralization from a serpentinite-derived lateritic regolith, Sulawesi Island, Indonesia:

592 Mineralogy, geochemistry and link to hydrologic flow regime. *J. Geochem. Explor.* 188, 240–  
593 256. <https://doi.org/10.1016/j.gexplo.2018.01.022>

594 Gautier, P., Quesnel, B., Boulvais, P., Cathelineau, M., 2016. The emplacement of the Peridotite  
595 Nappe of New Caledonia and its bearing on the tectonics of obduction: OBDUCTION IN NEW  
596 CALEDONIA. *Tectonics* 35, 3070–3094. <https://doi.org/10.1002/2016TC004318>

597 Golightly, J.P., 2010. Progress in Understanding the Evolution of Nickel Laterites, in: *The Challenge of*  
598 *Finding New Mineral Resources*<subtitle>Global Metallogeny, Innovative Exploration, and  
599 *New Discoveries*</SubTitle>. Society of Economic Geologists.  
600 <https://doi.org/10.5382/SP.15.2.07>

601 GPL software, 2021. CloudCompare.

602 Haldar, S.K., 2017. Deposits of Europe, in: *Platinum-Nickel-Chromium Deposits*. Elsevier, pp. 217–231.  
603 <https://doi.org/10.1016/B978-0-12-802041-8.00008-0>

604 Hatton, C.G., Main, I.G., Meredith, P.G., 1993. A comparison of seismic and structural measurements  
605 of scaling exponents during tensile subcritical crack growth. *J. Struct. Geol.* 15, 1485–1495.  
606 [https://doi.org/10.1016/0191-8141\(93\)90008-X](https://doi.org/10.1016/0191-8141(93)90008-X)

607 Iseppi, M., 2018. *Fracturation polyphasée et contrôles des gisements de nickel supergène de*  
608 *Nouvelle-Calédonie : Nouvelles méthodes d’exploration et modèles de gisements (PhD*  
609 *Thesis)*.

610 Iseppi, M., Sevin, B., Cluzel, D., Maurizot, P., Bayon, B.L., 2018. SUPERGENE NICKEL ORE DEPOSITS  
611 CONTROLLED BY GRAVITY-DRIVEN FAULTING AND SLOPE FAILURE, PERIDOTITE NAPPE, NEW  
612 CALEDONIA. *Econ. Geol.* 113, 531–544. <https://doi.org/10.5382/econgeo.2018.4561>

613 Jeanpert, J., 2017. *Structural and hydrogeologic characterization of the peridotitic massifs of New*  
614 *Caledonia (Theses)*. Université de la Réunion.

615 Jeanpert, J., Iseppi, M., Adler, P.M., Genthon, P., Sevin, B., Thovert, J.-F., Dewandel, B., Join, J.-L.,  
616 2019. Fracture controlled permeability of ultramafic basement aquifers. Inferences from the

617 Koniambo massif, New Caledonia. *Eng. Geol.* 256, 67–83.  
618 <https://doi.org/10.1016/j.enggeo.2019.05.006>

619 Join, J.-L., Robineau, B., Ambrosi, J.-P., Costis, C., Colin, F., 2005. Système hydrogéologique d'un  
620 massif minier ultrabasique de Nouvelle-Calédonie. *Comptes Rendus Geosci.* 337, 1500–1508.  
621 <https://doi.org/10.1016/j.crte.2005.08.011>

622 Kamb, W.B., 1959. Ice petrofabric observations from Blue Glacier, Washington, in relation to theory  
623 and experiment. *J. Geophys. Res.* 1896-1977 64, 1891–1909.  
624 <https://doi.org/10.1029/JZ064i011p01891>

625 Karperien, A., 2013. *FracLac for ImageJ*. NIH. <https://doi.org/10.13140/2.1.4775.8402>

626 Katayama, I., Abe, N., Hatakeyama, K., Akamatsu, Y., Okazaki, K., Ulven, O.I., Hong, G., Zhu, W.,  
627 Cordonnier, B., Michibayashi, K., Godard, M., Kelemen, P., the Oman Drilling Project Phase 2  
628 Science Party, 2020. Permeability Profiles Across the Crust-Mantle Sections in the Oman  
629 Drilling Project Inferred From Dry and Wet Resistivity Data. *J. Geophys. Res. Solid Earth* 125.  
630 <https://doi.org/10.1029/2019JB018698>

631 Lagabrielle, Y., Maurizot, P., Lafoy, Y., Cabioch, G., Pelletier, B., Régnier, M., Wabete, I., Calmant, S.,  
632 2005. Post-Eocene extensional tectonics in Southern New Caledonia (SW Pacific): Insights  
633 from onshore fault analysis and offshore seismic data. *Tectonophysics* 403, 1–28.  
634 <https://doi.org/10.1016/j.tecto.2005.02.014>

635 Leblanc, M., 1980. Chromite growth, dissolution and deformation from a morphological view point:  
636 SEM investigations. *Miner. Deposita* 15. <https://doi.org/10.1007/BF00206514>

637 Masihi, M., King, P.R., 2008. Connectivity Prediction in Fractured Reservoirs With Variable Fracture  
638 Size: Analysis and Validation. *SPE J.* 13, 88–98. <https://doi.org/10.2118/100229-PA>

639 Maurizot, P., Sevin, B., Lesimple, S., Bailly, L., Iseppi, M., Robineau, B., 2020. Chapter 10 Mineral  
640 resources and prospectivity of the ultramafic rocks of New Caledonia. *Geol. Soc. Lond. Mem.*  
641 51, 247–277. <https://doi.org/10.1144/M51-2016-17>

642 Muñoz, M., Ulrich, M., Cathelineau, M., Mathon, O., 2019. Weathering processes and crystal  
643 chemistry of Ni-bearing minerals in saprock horizons of New Caledonia ophiolite. *J.*  
644 *Geochem. Explor.* 198, 82–99. <https://doi.org/10.1016/j.gexplo.2018.12.007>

645 Myagkiy, A., Golfier, F., Truche, L., Cathelineau, M., 2019. Reactive Transport Modeling Applied to Ni  
646 Laterite Ore Deposits in New Caledonia: Role of Hydrodynamic Factors and Geological  
647 Structures in Ni Mineralization. *Geochem. Geophys. Geosystems* 20, 1425–1440.  
648 <https://doi.org/10.1029/2018GC007606>

649 Myagkiy, A., Truche, L., Cathelineau, M., Golfier, F., 2017. Revealing the conditions of Ni  
650 mineralization in the laterite profiles of New Caledonia: Insights from reactive geochemical  
651 transport modelling. *Chem. Geol.* 466, 274–284.  
652 <https://doi.org/10.1016/j.chemgeo.2017.06.018>

653 Niblack, W., 1986. *An introduction to digital image processing.*, Englewood Cliffs: Prentice-Hall. ed.

654 Pant, T., 2013. Effect of Noise in Estimation of Fractal Dimension of Digital Images. *Int. J. Signal*  
655 *Process. Image Process. Pattern Recognit.* 6, 101–116.  
656 <https://doi.org/10.14257/ijcip.2013.6.5.10>

657 Prinzhofer, A., Nicolas, A., Cassard, D., Moutte, J., Leblanc, M., Paris, J.P., Rabinovitch, M., 1980.  
658 Structures in the new caledonia peridotites-gabbros: Implications for oceanic mantle and  
659 crust. *Tectonophysics* 69, 85–112. [https://doi.org/10.1016/0040-1951\(80\)90128-6](https://doi.org/10.1016/0040-1951(80)90128-6)

660 Quesnel, B., de Veslud, C.L.C., Boulvais, P., Gautier, P., Cathelineau, M., Drouillet, M., 2017. 3D  
661 modeling of the laterites on top of the Koniambo Massif, New Caledonia: refinement of the  
662 per descensum lateritic model for nickel mineralization. *Miner. Deposita* 52, 961–978.  
663 <https://doi.org/10.1007/s00126-017-0712-1>

664 Quesnel, B., Gautier, P., Cathelineau, M., Boulvais, P., Couteau, C., Drouillet, M., 2016. The internal  
665 deformation of the Peridotite Nappe of New Caledonia: A structural study of serpentine-  
666 bearing faults and shear zones in the Koniambo Massif. *J. Struct. Geol.* 85, 51–67.  
667 <https://doi.org/10.1016/j.jsg.2016.02.006>

668 Reiss, M.A., Sabathiel, N., Ahammer, H., 2015. Noise dependency of algorithms for calculating fractal  
669 dimensions in digital images. *Chaos Solitons Fractals* 78, 39–46.  
670 <https://doi.org/10.1016/j.chaos.2015.07.004>

671 Roy, A., Perfect, E., Dunne, W.M., McKay, L.D., 2007. Fractal characterization of fracture networks:  
672 An improved box-counting technique. *J. Geophys. Res.* 112, B12201.  
673 <https://doi.org/10.1029/2006JB004582>

674 Santoro, L., Putzolu, F., Mondillo, N., Boni, M., Herrington, R., 2022. Trace element geochemistry of  
675 iron-(oxy)-hydroxides in Ni(Co)-laterites: Review, new data and implications for ore forming  
676 processes. *Ore Geol. Rev.* 140, 104501. <https://doi.org/10.1016/j.oregeorev.2021.104501>

677 Schindelin, J., Arganda-Carreras, I., Frise, E., Kaynig, V., Longair, M., Pietzsch, T., Preibisch, S., Rueden,  
678 C., Saalfeld, S., Schmid, B., Tinevez, J.-Y., White, D.J., Hartenstein, V., Eliceiri, K., Tomancak,  
679 P., Cardona, A., 2012. Fiji: an open-source platform for biological-image analysis. *Nat.*  
680 *Methods* 9, 676–682. <https://doi.org/10.1038/nmeth.2019>

681 Schnabel, R., Wahl, R., Klein, R., 2007. Efficient RANSAC for Point-Cloud Shape Detection. *Comput.*  
682 *Graph. Forum* 26, 214–226.

683 Sevin, B., Cluzel, D., Maurizot, P., Ricordel-Prognon, C., Chaproniere, G., Folcher, N., Quesnel, F.,  
684 2014. A drastic lower Miocene regolith evolution triggered by post obduction slab break-off  
685 and uplift in New Caledonia: Slab break-off in New Caledonia. *Tectonics* 33, 1787–1801.  
686 <https://doi.org/10.1002/2014TC003588>

687 Sevin, B., Ricordel-Prognon, C., Quesnel, F., Cluzel, D., Lesimple, S., Maurizot, P., 2012. First  
688 palaeomagnetic dating of ferricrete in New Caledonia: new insight on the morphogenesis  
689 and palaeoweathering of ‘Grande Terre’: First palaeomagnetic dating of ferricrete in New  
690 Caledonia. *Terra Nova* 24, 77–85. <https://doi.org/10.1111/j.1365-3121.2011.01041.x>

691 Tauler, E., Lewis, J.F., Villanova-de-Benavent, C., Aiglsperger, T., Proenza, J.A., Domènech, C.,  
692 Gallardo, T., Longo, F., Galí, S., 2017. Discovery of Ni-smectite-rich saprolite at Loma Ortega,  
693 Falcondo mining district (Dominican Republic): geochemistry and mineralogy of an unusual

694 case of “hybrid hydrous Mg silicate – clay silicate” type Ni-laterite. *Miner. Deposita* 52, 1011–  
695 1030. <https://doi.org/10.1007/s00126-017-0750-8>

696 Teitler, Y., Cathelineau, M., Ulrich, M., Ambrosi, J.P., Munoz, M., Sevin, B., 2019. Petrology and  
697 geochemistry of scandium in New Caledonian Ni-Co laterites. *J. Geochem. Explor.* 196, 131–  
698 155. <https://doi.org/10.1016/j.gexplo.2018.10.009>

699 Trescases, J., 1975. L'évolution géochimique supergène des roches ultrabasiques en zone tropicale:  
700 Formation des gisements nickélifères de Nouvelle-Calédonie: Mémoires ORSTOM (Office de  
701 la Recherche Scientifique et Technique Outre-Mer), in: Mémoires ORSTOM (Office de La  
702 Recherche Scientifique et Technique Outre-Mer).

703 Tutolo, B.M., Mildner, D.F.R., Gagnon, C.V.L., Saar, M.O., Seyfried, W.E., 2016. Nanoscale constraints  
704 on porosity generation and fluid flow during serpentinization. *Geology* 44, 103–106.  
705 <https://doi.org/10.1130/G37349.1>

706 USGS, 2022. Mineral Commodity Summaries 2022.

707 Villanova-de-Benavent, C., Proenza, J.A., Galí, S., García-Casco, A., Tauler, E., Lewis, J.F., Longo, F.,  
708 2014. Garnierites and garnierites: Textures, mineralogy and geochemistry of garnierites in  
709 the Falcondo Ni-laterite deposit, Dominican Republic. *Ore Geol. Rev.* 58, 91–109.  
710 <https://doi.org/10.1016/j.oregeorev.2013.10.008>

711 Walsh, J.J., Watterson, J., 1993. Fractal analysis of fracture patterns using the standard box-counting  
712 technique: valid and invalid methodologies. *J. Struct. Geol.* 15, 1509–1512.  
713 [https://doi.org/10.1016/0191-8141\(93\)90010-8](https://doi.org/10.1016/0191-8141(93)90010-8)

714

## 715 Appendix A

### 716 CT acquisition

717 The CT methodology drives the resolution of each sample. Indeed, it is mainly determined by the fixed  
718 number of detectors and the size of the analyzed sample. The bigger the sample is, the lower the  
719 resolution is since each detector analyses signal for a more significant part of the sample. Thus, a  
720 resolution of 65  $\mu\text{m}/\text{vx}$  was obtained by using a voltage of 120 kV and a current of 110  $\mu\text{A}$  for the core  
721 sample, and 12.5 $\mu\text{m}/\text{vx}$  using a voltage of 85 kV and a current of 95  $\mu\text{A}$  for S\_2.

### 722 Features extraction

#### 723 1. *Image stacks analysis*

724 The first step of the structural features extraction is based on image analyses on FIJI. A local auto  
725 threshold computed for each pixel within a set radius was applied using the Niblack method (Niblack,  
726 1986). Based on the standard deviation calculation, this method highlights significant changes in grey  
727 values and thus reveals the microfracture network. Then, successive median filters were applied to  
728 reduce the noise until the visual aspect of the images was estimated to be correct. The resulting images  
729 were then skeletonized to describe the microfractures better. Indeed, this method removes pixels  
730 repeatably from the edges of objects (in current work, the fractures) until they are reduced to single  
731 pixel-wide skeletons, allowing them to be identified.

#### 732 2. *Point cloud analysis*

733 On CloudCompare, the point cloud was first sub-sampled randomly to reduce its size for computing  
734 costs. Then, the normal vector for each point was calculated through the Hough Normal Computation  
735 Plugin (Boulch and Marlet, 2012). This plugin estimates the normal by finding the best one in a  
736 neighbourhood around a chosen point. Then, the normal is converted into a dip/dip direction scale  
737 factor to colorize the point cloud. Distinct fracture sets were identified based on the dip and dip  
738 direction distribution, and each point was assigned to a given set. Finally, planes were adjusted from

739 points using the Ransac Shape Detection Plugin (Schnabel et al., 2007) and exported to analyze their  
740 spatial and orientation distribution.

#### 741 Fractal dimension analysis

742 Since fractal analysis is noise sensitive, a prerequisite for evaluating the potential fractal organization  
743 of fractures, is to reduce unwanted noise, hence allowing a better extract of the structural features  
744 (Pant, 2013; Reiss et al., 2015). The background noise of CT images was thus treated with FIJI by  
745 applying a local auto threshold with the Niblack method, followed by an outlier removal through the  
746 analyze particle plugin and a skeletonize step. Then the fractal dimension of the fracture network was  
747 calculated by the box-counting method (Roy et al., 2007) using the FraCLac plugin (Karperien, 2013).  
748 The box sizes vary from 1 pixel to 45% of the height of the images to avoid errors in the estimation  
749 (Walsh and Watterson, 1993). Furthermore, to reduce the bias related to the grid location (Roy et al.,  
750 2007), 50 different positions were used for each image, and the final fractal dimension corresponds to  
751 their mean value. The calculation was restricted to only a central portion of S\_2 to avoid disturbances  
752 from part of the image outside the sample.

#### 753 [References to appendix A.](#)

754 Boulch, A., Marlet, R., 2012. Fast and Robust Normal Estimation for Point Clouds with Sharp Features.  
755 Comput. Graph. Forum 31, 1765–1774. <https://doi.org/10.1111/j.1467-8659.2012.03181.x>

756 Karperien, A., 2013. FraCLac for ImageJ. NIH. <https://doi.org/10.13140/2.1.4775.8402>

757 Niblack, W., 1986. An introduction to digital image processing., Englewood Cliffs: Prentice-Hall. ed.

758 Pant, T., 2013. Effect of Noise in Estimation of Fractal Dimension of Digital Images. Int. J. Signal  
759 Process. Image Process. Pattern Recognit. 6, 101–116.

760 <https://doi.org/10.14257/ijcip.2013.6.5.10>

761 Reiss, M.A., Sabathiel, N., Ahammer, H., 2015. Noise dependency of algorithms for calculating fractal  
762 dimensions in digital images. Chaos Solitons Fractals 78, 39–46.

763 <https://doi.org/10.1016/j.chaos.2015.07.004>

764 Roy, A., Perfect, E., Dunne, W.M., McKay, L.D., 2007. Fractal characterization of fracture networks:  
765 An improved box-counting technique. *J. Geophys. Res.* 112, B12201.  
766 <https://doi.org/10.1029/2006JB004582>

767 Schnabel, R., Wahl, R., Klein, R., 2007. Efficient RANSAC for Point-Cloud Shape Detection. *Comput.*  
768 *Graph. Forum* 26, 214–226.

769 Walsh, J.J., Watterson, J., 1993. Fractal analysis of fracture patterns using the standard box-counting  
770 technique: valid and invalid methodologies. *J. Struct. Geol.* 15, 1509–1512.  
771 [https://doi.org/10.1016/0191-8141\(93\)90010-8](https://doi.org/10.1016/0191-8141(93)90010-8)

772